Journal of the Taiwan Institute of Chemical Engineers 171 (2025) 106033

Contents lists available at ScienceDirect

Journal of the Taiwan Institute of Chemical Engineers

journal homepage: www.journals.elsevier.com/journal-of-the-taiwan-institute-of-chemical-engineers

High-performance electrochemical sensors with $SnBi_2O_3$/Graphene oxide nanocomposite for selective antibiotic detection

Krishnanpandi Alagumalai [a,1], Nandhini Munusamy [b,1], Shen Ming Chen [b,*], Alangadu Kothandan Vivekanandan [c,d], Shih-Hsun Chen [d], Mani Sivakumar [e,*], Seong-Cheol Kim [a,*], B. Prakash [f]

[a] School of chemical engineering, Yeungnam University, Gyeongsang 38541, Republic of Korea
[b] Department of Chemical Engineering and Biotechnology, College of Engineering, National Taipei University of Technology, No. 1, Chung-Hsiao East Road, Section 3, Taipei 10608, Taiwan
[c] Department of Aeronautical Engineering, Annasaheb Dange college of Engineering and technology, Ashta, Sangli, 416301, Maharashtra, India
[d] Department of Mechanical Engineering, National Yang Ming Chiao Tung University, Hsinchu 300039, Taiwan
[e] Department of Chemical Engineering, Faculty of Engineering, Mahidol University, Nakhon, Pathom, 73170, Thailand
[f] Department of Biotechnology, School of Life Sciences Vels Institute of Science, Technology and Advanced Studies (VsISTAS) Pallavaram, Chennai, Tamil Nadu, India

ARTICLE INFO

Keywords:
$SnBi_2O_3$/GO composite
Nitrofurans
Electrochemical sensor
Bio-fluids and water samples

ABSTRACT

Background: Environmental contaminants like nitrofurans (NF) can be detected using rapid, sensitive, and efficient monitoring techniques. However, ineffective detection systems delay responses, allowing contaminants to persist in the environment, increasing their toxicity, and causing long-term harm to ecosystems and human health. An alternative is the electrochemical method for NF detection, which is fast, cost-effective, and reliable.
Methods: We developed a low-cost, portable nanocomposite material, Sn-Bi_2O_3/GO, for the detection of NF, marking its first reported use. The crystallinity, functional groups, surface structure, and oxidation states of the materials were analyzed through various analytical and spectroscopic techniques.
Significant findings: $SnBi_2O_3$/GO composites modified glassy carbon electrode (GCE) surface was employed to detect NF using cyclic voltammetry (CV) and differential pulse voltammetry (DPV). Then, the $SnBi_2O_3$/GO/GCE showed outstanding selectivity, even in the presence of interfering substances, with a wide linear detection range from 0.023 μM to 814.36 μM, a detection limit (LOD) of 0.0124 μM (S/N = 3), and an ultra-sensitivity of 2.857 μA μM^{-1} cm^{-2}. Additionally, the $SnBi_2O_3$/GO/GCE successfully detected NF in biofluids and water samples, demonstrating satisfactory accuracy and recovery.

1. Introduction

Environmental pollution has become a pressing concern, with far-reaching consequences for human health and the ecosystem. The release of pollutants into the environment can have devastating effects on aquatic life, soil, and air quality [1–5]. Pollutants can be broadly classified into two main categories: chemical and biological pollutants. Chemical pollutants, such as heavy metals, pesticides, synthetic antibiotics, and industrial chemicals, can enter the environment through human activities such as industrial processes, agriculture, and waste disposal [6–11]. Biological pollutants, on the other hand, include microorganisms such as bacteria, viruses, and fungi that can cause disease in humans and animals [12–14]. The overuse of antibiotics in modern healthcare has increasingly threatened the environment, with severe consequences for human health and the ecosystem. Antibiotics are widely used in medicine, livestock, and even agriculture, however, their improper disposal and misuse have led to their entry into the environment [15–17]. This occurs primarily through wastewater treatment plants, agricultural runoff, and surface water. Once in the environment, antibiotics can persist for extended periods and contaminate soil, water, and air. Antibiotic exposure has been linked to antibiotic-resistant bacteria, which can cause serious infections in humans and animals [18–20]. One class of antibiotics that has been particularly concerning is nitrofurans (NF), which have been detected in waterways and

* Corresponding authors.
E-mail addresses: smchen1957@gmail.com (S.M. Chen), sivaphy05@gmail.com (M. Sivakumar), sckim07@ynu.ac.kr (S.-C. Kim).
[1] These authors contributed equally

https://doi.org/10.1016/j.jtice.2025.106033
Received 28 October 2024; Received in revised form 13 February 2025; Accepted 15 February 2025
Available online 9 March 2025

wastewater around the world.

NF are synthetic antibiotics used to treat urinary tract infections, but they have been shown to persist in the environment for extended periods, posing a risk to aquatic life [21–23]. The toxicity of NFs is associated with their ability to disrupt normal cellular processes, causing adverse effects on reproduction, growth, and development [24,25]. Moreover, the lack of effective monitoring and detection methods can lead to a delayed response to pollution incidents, causing irreparable damage to the environment [5,26]. Therefore, there is a pressing need for the development of reliable and efficient monitoring and detection methods to identify pollutants, especially antibiotics, in the environment. Techniques such as gas chromatography-mass spectrometry (GC–MS) [27] and liquid chromatography-tandem mass spectrometry (LC-MS/MS) [28] have been widely used for the detection of pollutants in environmental samples. Additionally, sensor technologies, such as electrochemical and optical sensors, have shown significant promise in real-time pollutant detection [29,30].This current work emphasises electrochemical sensors.

The development of electrochemical sensors has revolutionised the field of analytical chemistry, enabling the detection of various analytes with high sensitivity and selectivity [31–33]. Electrochemical sensors utilize a working electrode and a counter electrode to detect changes in electrical current or potential induced by the presence of target analytes, such as antibiotics. In recent years, various electrochemical sensors have been developed for detecting antibiotics in foods, including amperometric [34] and impedimetric sensors [35]. The use of nanomaterials as coatings for electrochemical sensors has further enhanced their performance, allowing for improved detection limits and reduced sample volumes [36]. Nanoparticles have been increasingly used in electrochemical sensors in recent years due to their unique properties, such as high surface-to-volume ratio, tunable size, and tailored surface chemistry. These properties enable nanoparticles to enhance the sensitivity, selectivity, and stability of electrochemical sensors [37–39]. Several types of nanoparticles have been explored for electrochemical sensing applications, including metal nanoparticles (Au, Ag, Pt), metal oxide nanoparticles (TiO_2, SnO_2), and carbon-based nanoparticles (CNTs, graphene) [40,41].

Among the various materials used for electrochemical sensors, tin bimuth oxide ($SnBi_2O_3$) has shown promising results due to its excellent electrochemical properties, better electrical conductivity, and higher mechanical strength, which make it an ideal candidate for the development of electrochemical sensors and biocompatibility [42,43]. $SnBi_2O_3$ is a metal oxide-based material that has been extensively studied for its potential applications in electrochemical sensing. The surface morphology, particle size, and crystal structure of the material influence the sensor's performance [44,45]. The electrochemical properties of $SnBi_2O_3$ have been studied using various techniques, including cyclic voltammetry and impedance spectroscopy [46]. These techniques have revealed that $SnBi_2O_3$ exhibits a reversible redox reaction, which is responsible for excellent electrochemical performance [47,48]. The detection mechanism of analytes like antibiotics using $SnBi_2O_3$-based sensors involves the oxidation or reduction reaction of the analyte at the surface of the electrode material [49–51]. While $SnBi_2O_3$ has several advantages in electrochemical sensors, such as good catalytic activity and stability, there are a few potential disadvantages that could arise depending on the specific application like limited conductivity, aggregation of nanoparticles, slow electron transfer kinetics, and surface fouling [52,53]. To further improve its electrochemical performance of $SnBi_2O_3$, combined with graphene oxide (GO) [54]. GO has gained significant attention in electrochemical applications due to its exceptional conductivity, large surface area, and the presence of oxygen-containing functional groups [55–57]. These functional groups facilitate better dispersion of nanoparticles and improve electron transfer processes. When combined with $SnBi_2O_3$ nanoparticles, GO serves as an excellent support matrix, offering more active sites for the electrochemical reaction and enhancing the sensitivity and selectivity of NF detection [58]. The composite structure of $SnBi_2O_3$/GO provides a synergistic effect, leading to improved electrochemical response, which makes it a promising candidate for detecting NF in complex matrices such as biological and environmental samples [59,60]. Given that no research has yet focused on this specific composite for NF detection, our study seeks to fill this gap, providing a new approach to electrochemical sensor development.

In the present study, $SnBi_2O_3$ nanoparticles were synthesized through a two-stage procedure. The $SnBi_2O_3$/GCE electrochemical sensor was fabricated using the synthesized nanoparticles, and its effectiveness was subsequently examined through extensive analytical testing and measurements. The electrochemical sensor performance was evaluated through cycliv voltametry (CV) and differential pulse voltammetry (DPV) techniques, followed by electrochemical impedance spectroscopy. The parameters such as repeatability, reproducibility, and stability were evaluated across different pH ranges and cyclic voltages. Additionally, real sample analysis was conducted using, human urine, and tap water.

2. Experimental section

2.1. Chemicals and reagents

Tin (II) chloride ($SnCl_2$), bismuth (III) nitrate pentahydrate ($Bi(NO_3)_3{\cdot}5H_2O$), hydroxylamine hydrochloride ($NH_2OH.HCl$) and nitrofurazone ($C_6H_6N_4O_4$) were bought from Sigma Aldrich. Glucose (GLU), dopamine (DOP), ascorbic acid (AA), N-acetyl-p-aminophenol (APAP), chloramphenicol (CAP), potassium (K^+), calcium (Ca^{2+}), magnesium (Mg^{2+}), sodium Na^+), and zinc (Zn^{2+}) were procured from Sigma-Aldrich and used and were of analytical grade. For the electrochemical experiments, the phosphate buffer solution was made by using sodium phosphate dibasic anhydrous (NaH_2PO_4; ≥99.0 %), sodium phosphate monobasic dihydrate ($NaH_2PO_4{\cdot}2H_2O$; <100 %), with adjusting 0.1 M HCl (HCl; ≥37 %) and sodium hydroxide (NaOH; ≥98 %), Potassium ferricyanide ($K_3Fe(CN)_6$, >98 %) and potassium ferrocyanide ($K_4Fe(CN)_6{\cdot}3H_2O$, >99 %) from Duksan (Taiwan). Alumina powder (α-Al_2O_3; 0.05μm) and ethanol (C_2H_5OH; >95 %) were bought from Struers (Taiwan) and Taiwan Sugar Corporation. All the chemicals were utilized in double distilled water to make the required solutions. All the chemicals were analytical grade and used without further purification.

2.2. Synthesis of $SnBi_2O_3$ nanoparticles

The $SnBi_2O_3$ nanoparticles were synthesized using a two-stage process. In the first stage, 1.0 M bismuth nitrate pentahydrate was dissolved in 40 mL of deionized (DI) water while stirring vigorously for 15 mins. Subsequently, 15 mL of a 1.0 M tin chloride solution was added to the mixture, followed by the addition of 10 mL of 0.5 M hydrochloric acid (HCl). The reaction mixture was then heated to 60 °C for 20 mins, and the pH was adjusted to 12 using 1.0 M sodium hydroxide (NaOH). The resulting brown solution was transferred to a Teflon-lined autoclave for hydrothermal treatment at 180 °C for 12 h. Afterwards, the precipitated material was collected via centrifugation, washed with DI water and ethanol, and dried in a hot air oven at 80 °C for 6 h. Finally, the material was calcined at 400 °C for 2 h to yield tin bismuth oxide, which is referred to as $SnBi_2O_3$ throughout the manuscript, as illustrated in Scheme 1(a).

2.3. Synthesis of $SnBi_2O_3$/GO nanocomposites

The $SnBi_2O_3$/GO composite was synthesized using an ultrasonication technique. Initially, GO was prepared from natural graphite powder following a modified Hummers' method [61]. For the composite synthesis, 0.05 g of GO and 0.5 g of $SnBi_2O_3$ were each separately dispersed in DI water and subjected to ultrasonication for 30 mins to ensure

uniform dispersion. The dispersed GO was then combined with the $SnBi_2O_3$ solution, and the mixture underwent an additional 30 mins of ultrasonication to achieve thorough integration of the GO with $SnBi_2O_3$. The resulting composite was washed with DI water and ethanol and then dried at 55 °C (Scheme 1 (b)).

2.4. Fabrication of $SnBi_2O_3$/GO on GCE

The glassy carbon electrode (GCE) was initially cleaned through ultrasonication in deionized (DI) water for 5 mins to remove any surface impurities. Subsequently, the GCE was polished with a 0.05 μm alumina slurry, followed by thorough rinsing with DI water and ethanol to ensure complete removal of polishing residues. After polishing, the electrode was dried in a hot air oven, resulting in a smooth, mirror-like surface. For the preparation of the nanocomposite, 5 mg of $SnBi_2O_3$/GO was dispersed in 1 mL of DI water and sonicated for 20 mins to achieve a uniform suspension. A 6 μL aliquot of this $SnBi_2O_3$/GO suspension was carefully drop-cast onto the cleaned GCE surface and allowed to air dry at room temperature, facilitating the formation of a stable layer (Scheme 1 (b)). Following the fabrication process, the modified $SnBi_2O_3$/GO/GCE was rinsed with DI water to eliminate any loosely bound particles. This $SnBi_2O_3$/GO-modified GCE was then utilized for the electrochemical detection of NF. For comparative analysis, similar experiments were conducted using $SnBi_2O_3$/GCE and GO/GCE under identical experimental conditions.

2.5. Instrumentation

Powder X-ray diffraction (PXRD) analysis was conducted using a PANalytical B.V. diffractometer with a monochromatic Cu-Kα source and a PIXcel3D detector. Fourier transform infrared (FT-IR) spectroscopy was performed using a JASCO FT/IR-6600 instrument, while Raman spectroscopy was carried out using a Raman Dong Woo 500 I (Korea). Field emission scanning electron microscopy (FE-SEM) images were acquired with a Hitachi S-3000H equipped with an energy-dispersive X-ray (EDX) spectrometer for elemental mapping. Transmission electron microscopy (TEM) images were obtained from a JEOL-JEM-2100F, which also provided selected area electron diffraction (SAED) patterns. X-ray photoelectron spectroscopy (XPS) analysis was conducted using a Thermo ESCALAB 250 instrument.

Electrochemical impedance spectroscopy (EIS) was performed using an Admiral Instruments Squidstat Plus Potentiostat (1709 CH1) over a frequency range of 10–100 Hz with a 10 mV potential in a 5.0 mM $[Fe(CN)_6]^{3-/4-}$ solution containing 0.1 M KCl. Electrochemical sensor performance was evaluated using cyclic voltammetry (CV) and differential pulse voltammetry (DPV) with CHI 1205B and CHI 900 workstations (CHI Instruments, Inc., USA) under ambient conditions. A three-electrode setup was employed, consisting of an Ag/AgCl reference electrode, a glassy carbon electrode (GCE, 0.071 cm^2 area) as the working electrode, and a platinum wire counter electrode (ALS Co., Ltd, Japan). Prior to analysis, the electrolyte solutions were deoxygenated by purging with nitrogen gas for 15 mins.

3. Results and discussion

3.1. Crystal structure and surface analysis

In Fig. 1A, the XRD patterns of $SnBi_2O_3$, GO, and $SnBi_2O_3$/GO composites were analysed to investigate crystal formation and space group. The XRD pattern of the synthesized $SnBi_2O_3$ composite was analysed by matching the diffraction peaks with reference patterns due to the absence of a specific JCPDS file for $SnBi_2O_3$. The peaks corresponding to

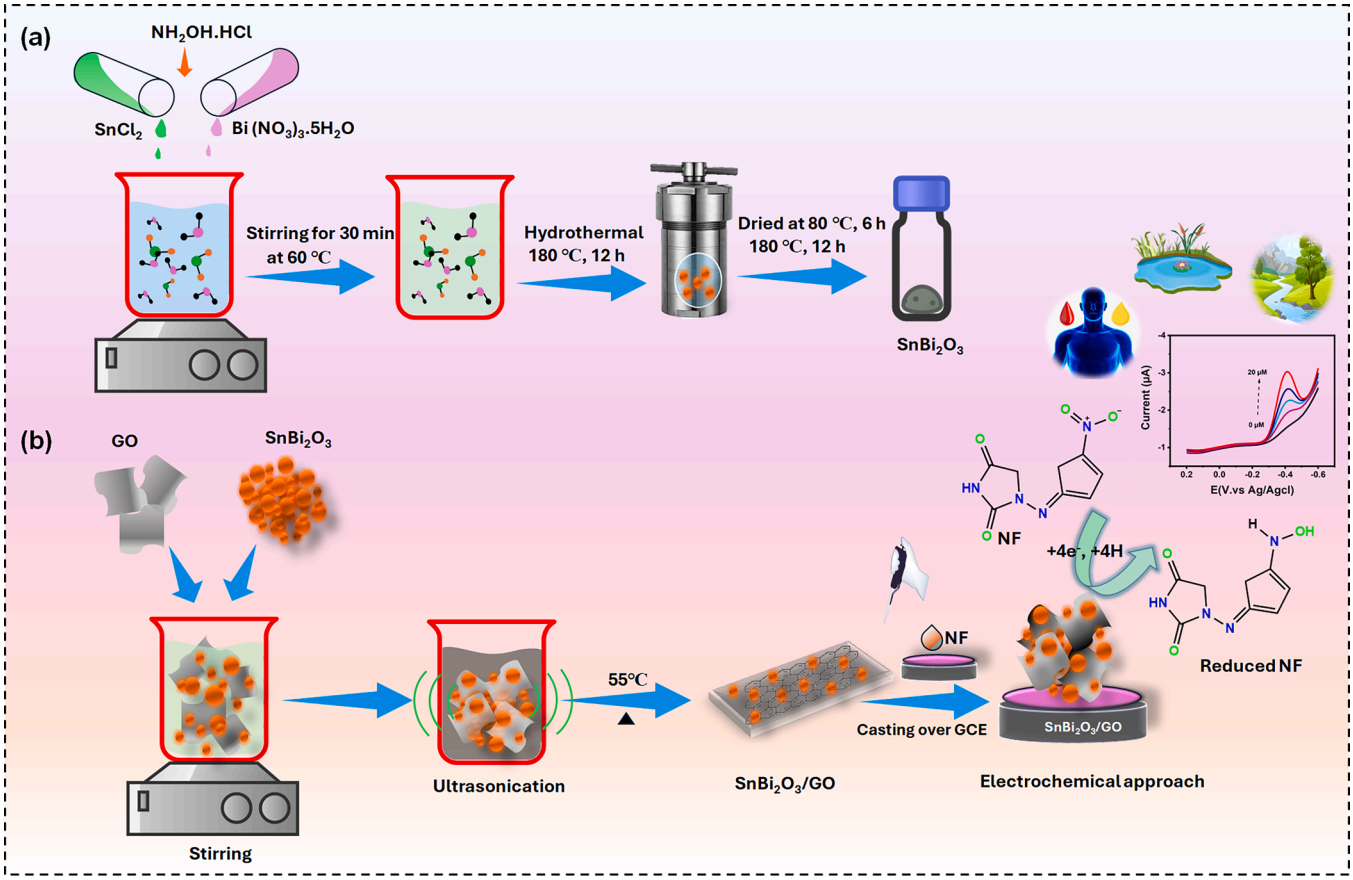

Scheme 1. Synthesis process of $SnBi_2O_3$ nanoparticle and $SnBi_2O_3$/GO nanocomposites for electrochemical detection of NF.

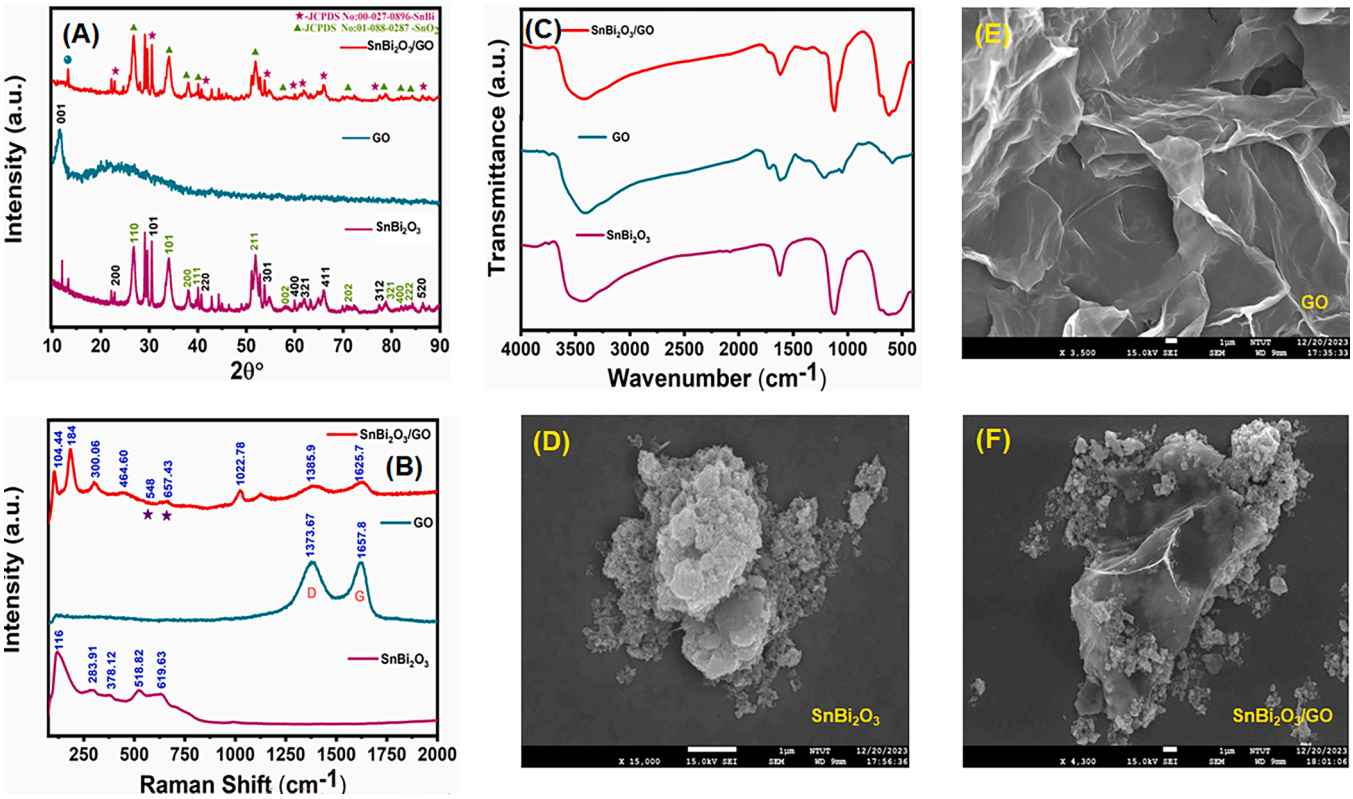

Fig. 1. (A) Pro-XRD, (B) Raman, (C) FT-IT analysis for $SnBi_2O_3$, GO and $SnBi_2O_3$/GO. FE-SEM images of (D) $SnBi_2O_3$, (E) GO and (F) $SnBi_2O_3$/GO composites.

the SnBi phase were indexed using JCPDS No: 00–027–0899, with prominent reflections observed at 22.8° (200), 30.5° (101), 40.6° (220), 53.7° (301), 60.0° (400), 61.8° (321), 66.1° (411), 77.4° (312), and 86.6° (520). Additionally, peaks corresponding to SnO_2 were identified and matched with JCPDS No: 01–088–0287, appearing at 26.7° (110), 34.1° (101), 38.1° (200), 40.0° (111), 51.8° (211), 58.0° (002), 70.8° (202), 79.0° (321), 82.1° (400), and 84.4° (222). The presence of characteristic peaks from both SnBi and SnO_2 phases confirms the successful synthesis of the $SnBi_2O_3$ composite, with possible interactions between the two phases influencing the structural properties of the material. For GO, peaks were observed at a 2θ value of 11.59°, corresponding to the (002) lattice plane, confirming the well-defined oxygen functionality on the GO nanolayer surface. In the $SnBi_2O_3$/GO composite, a slight shift in the 2θ peaks was observed, indicating polar-polar interactions between $SnBi_2O_3$ and GO, which increased the number of oxygen molecules in the composite. This shift suggests strong interfacial bonding between the two components, further supporting the successful integration of GO within the $SnBi_2O_3$ matrix [62]. These interactions may enhance the structural stability and improve the functional properties.

The Raman spectra of $SnBi_2O_3$, GO, and $SnBi_2O_3$/GO composites are presented in Fig. 1B. The Bi_2O_3 peak at 116.19 cm^{-1} originates from the Ag symmetry, primarily due to the participation of Bi atoms. Peaks at 283.91 cm^{-1} and 378.12 cm^{-1} are attributed to the metal state displacements of O atoms in α-Bi_2O_3 and unique Bi–O stretching vibrations, respectively [63]. The peak at 518.82 cm^{-1} is attributed to the B_2g mode, which is typically associated with bending vibrations within the SnO_2 lattice structure, while the prominent peak at 619.63 cm^{-1} corresponds to the A_1g mode, characteristic of symmetric Sn–O bond stretching vibrations, a defining feature of the rutile phase of SnO_2. For graphite-derived GO, two prominent peaks were observed at 1373.67 cm^{-1} and 1657.8 cm^{-1}, corresponding to an I_D/I_G ratio of 1.2, confirming the successful formation of GO with oxygen functionality. In the $SnBi_2O_3$/GO composites, the prominent peaks were observed at 104.44 cm^{-1}, 184.10 cm^{-1}, 300.06 cm^{-1}, 464.60 cm^{-1}, 548 cm^{-1}, 657.43 cm^{-1}, 1022.78 cm^{-1}, 1385.94 cm^{-1}, and 1625.72 cm^{-1}. Notably, the characteristic peaks of 518.82 cm^{-1} and 619.63 cm^{-1}, corresponding to SnO_2, exhibited slight shifts to 548 cm^{-1} and 657.43 cm^{-1}, respectively. These shifts, along with a decrease in peak intensity, can be attributed to the interactions between $SnBi_2O_3$ and GO. The disorder introduced by these interactions suggests the formation of metal-carbon and metal-oxygen bonds, which confirm the successful integration of $SnBi_2O_3$ and GO into a composite structure. This structural modification highlights the effective hybridization of the components in the $SnBi_2O_3$/GO composite.

The weak and broad peak observed in the range of 439.7 cm^{-1} to 831.1 cm^{-1} is associated with the formation of metal-oxygen (M–O) bonds, specifically, Sn–O and Bi–O bonds (Fig. 1C). The peak at 1123.3 cm^{-1} is attributed to the Bi–O stretching vibrations, indicating the presence of Bi–O bonds within the $SnBi_2O_3$ structure [64]. Additionally, the appearance of a weak and broad peak at 1621 cm^{-1} and 3445.6 cm^{-1} is likely attributed to the bending vibrations of adsorbed water molecules and hydroxyl ions residing on the surface of the $SnBi_2O_3$ [65]. The FT-IR spectrum of GO exhibits several key characteristic peaks at 3401 cm^{-1}, 1398 cm^{-1}, and 1062 cm^{-1}, which correspond to the following vibrational modes: the broad peak at 3401 cm^{-1} is attributed to the hydroxyl stretching vibrations (C–OH), the peak at 1398 cm^{-1} is related to the deformation of OH groups in C–OH and the peak at 1062 cm^{-1} corresponds to the stretching vibrations of C–O. These peaks are indicative of the oxygen-containing functional groups present on the surface of GO, which are critical for its chemical reactivity and interactions with other materials [66]. The FT-IR spectrum of $SnBi_2O_3$/GO exhibits multiple characteristic peaks, clearly indicating the presence of both $SnBi_2O_3$ and GO within the composite. These distinct peaks correspond to the functional groups and bonds associated with each component, providing strong evidence of their successful integration. Consequently, the FT-IR analysis further validates the successful synthesis and formation of the $SnBi_2O_3$/GO composite.

The FE-SEM images of $SnBi_2O_3$, GO, and $SnBi_2O_3$/GO composites

reveal distinct morphologies shown in Fig. 1(D-F). $SnBi_2O_3$ nanoparticles appear well-formed and uniformly distributed. GO exhibits its characteristic ultra-thin, sheet-like structure, highlighting its excellent film-forming ability. In the $SnBi_2O_3$/GO composite, the nanoparticles are homogeneously dispersed across GO sheets due to ultrasonic agitation and host-guest interactions [17]. This intermingled structure demonstrates strong synergy between the materials, enhancing the composites properties for potential applications.

The survey spectrum of the $SnBi_2O_3$/GO composites, shown in Fig. 2A, confirms the presence of elemental components. Elemental fitting analysis verifies the interactions between metal states and functional groups with metal and heteroatoms. In Fig. 2B, the Bi 4f spectrum displays two major peaks: at 166.2 eV and 165.1 eV (Bi $4f_{5/2}$) and at 160.9 eV and 159.2 eV (Bi $4f_{7/2}$), respectively. Fig. 2C shows the Sn 3d fitting, with two main peaks at 488.5 eV (Sn $3d_{5/2}$) and 496.9 eV (Sn $3d_{3/2}$), confirming the formation of the Sn 3d state with a peak difference of 8.4 eV. Likewise, the GO component, as seen in Fig. 2D, exhibits peaks at 285.9 eV and 287.6 eV, corresponding to the C—C and O=C—O bonding positions. In Fig. 2E, the oxygen peaks at 530.8 eV and 531.9 eV are attributed to metal-oxygen (O-M) and carbon-oxygen (O—C) interactions, respectively. These findings confirm the elemental composition and interactions in the $SnBi_2O_3$/GO composites.

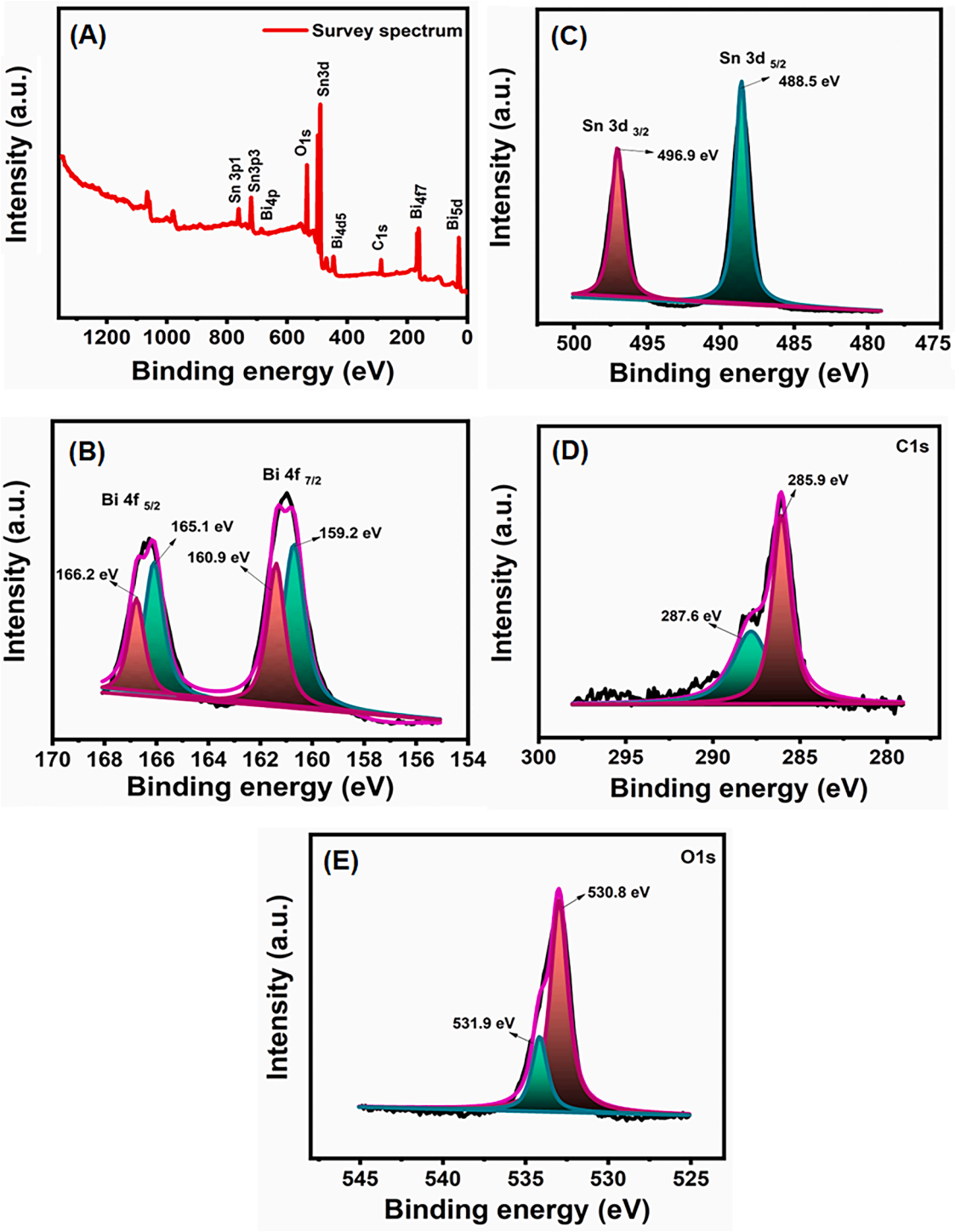

Fig. 2. (A) Survey spectrum of $SnBi_2O_3$/GO, Individual XPS spectrum of (B) Bi 4f, (C) Sn 3d (D) C 1 s, (E) O 1s.

3.2. Electrochemical application

3.2.1. Electrochemical impedance spectroscopy studies

EIS was employed to evaluate the electrical conductivity of Bare-GCE, $SnBi_2O_3$, GO, and the $SnBi_2O_3$/GO composite, using a 5 mM solution of $[Fe(CN)_6]^{3-/4-}$ in 0.5 M KCl as the supporting electrolyte. In Fig. 3A presents the Nyquist plot (Z_{im} vs. Z_{re}) for Bare GCE, $SnBi_2O_3$/GCE, GO/GCE, and $SnBi_2O_3$/GO/GCE. The semicircle observed in the low-frequency region corresponds to the charge-transfer resistance (R_{ct}), while the high-frequency region represents the electrolyte diffusion process. Generally, the radius of the semicircle is directly related to the material's resistance. Based on the EIS data, critical parameters such as series resistance (R_s), charge transfer resistance (R_{ct}), and capacitance (C) were evaluated and presented in Table 1 [67,68]. Among the electrodes examined, the $SnBi_2O_3$/GO/GCE demonstrated the lowest R_{ct}, indicating superior conductivity and significantly improved charge transfer efficiency compared to Bare GCE, $SnBi_2O_3$/GCE, and GO/GCE individually.

The electrochemical properties of the Bare GCE, $SnBi_2O_3$/GCE, GO/GCE, and $SnBi_2O_3$/GO/GCE electrodes were investigated using CV in a 5 mM $[Fe(CN)_6]^{3-/4-}$ solution with 0.5 M KCl as the supporting electrolyte. The different redox peaks (I_{pa}/I_{pc}) were observed for the Bare GCE ($I_{pa}/I_{pc} = 0.963$), GO/GCE ($I_{pa}/I_{pc} = 0.980$), $SnBi_2O_3$/GCE ($I_{pa}/I_{pc} = 1.002$), and $SnBi_2O_3$/GO/GCE ($I_{pa}/I_{pc} = 0.978$), as seen Fig. 3B. Among these, the $SnBi_2O_3$/GO/GCE electrode exhibited the highest redox peak currents, indicating superior electrochemical activity. This enhanced performance can be attributed to the $SnBi_2O_3$/GO composite providing a greater number of electroactive sites compared to $SnBi_2O_3$ or GO alone. The well-dispersed $SnBi_2O_3$ nanoparticles within the GO matrix facilitate more efficient electron transfer and offer an increased number of reactive sites for the electrochemical process. Furthermore, the electroactive surface area of Bare GCE, $SnBi_2O_3$/GCE, GO/GCE, and $SnBi_2O_3$/GO/GCE were calculated by Randles Sevcik Eq. (1) [69].

Table 1
Electrochemical impedance parameters of various electrodes.

Name of modified electrode	$R_s(\Omega)$	$R_{ct}(\Omega)$	A(cm^2)	v(m V/s)
Bare GCE	117	871	0.114	0.05
$SnBi_2O_3$//GCE	117	652	0.117	0.05
GO/GCE	149	510	0.115	0.05
$SnBi_2O_3$//GO/GCE	146	248	0.141	0.05

$$I_{pa} = 2.69 \times 105AD1/2n3/2v1/2C \quad (1)$$

I_{pa}means the peak current (μA), A signifies the active surface area (cm^2), D is the diffusion coefficient of the electrolyte solution, n represents the number of electrons transferred ($n = 1$), υ indicates the scan rate (V/s), and C stands for the concentration of the electrolyte solution (5 mM)) was used to calculate the active surface area of the modified electrodes using the anodic slope from the linear plot, as seen in Fig. S1 (A-H). Using this equation, the estimated electroactive surface area (EASA) was found to be 0.114, 0.117, 0.115, and 0.141 cm^2 for the Bare GCE, $SnBi_2O_3$/GCE, GO/GCE, and $SnBi_2O_3$/GO/GCE, respectively. These results indicate that the $SnBi_2O_3$/GO/GCE exhibits the highest EASA and the most efficient electron transfer among the tested electrodes.

3.2.2. Electrochemical behaviour of $SnBi_2O_3$/GO/GCE towards NF

Fig. 3C illustrates the CV response of various modified electrodes, including Bare GCE, $SnBi_2O_3$/GCE, GO/GCE, and $SnBi_2O_3$/GO/GCE, in 0.05 M PBS (pH 7.0) containing 250 μM NF at a scan rate of 50 mV/s. The $SnBi_2O_3$/GO/GCE electrode exhibited the highest reduction peak current of approximately −11.83 μA at a potential of −0.46 V, compared to Bare GCE, $SnBi_2O_3$/GCE, and GO/GCE, which showed peak currents of −8.66 μA, −9.06 μA, and −10.68 μA at potentials of −0.44 V, −0.45 V, and −0.46 V, respectively. However, the individual Bi_2O_3 and SnO_2 were combined with GO (Bi_2O_3/GO and SnO_2/GO) and examined under the same experimental working conditions, as seen in Fig. S2. The results

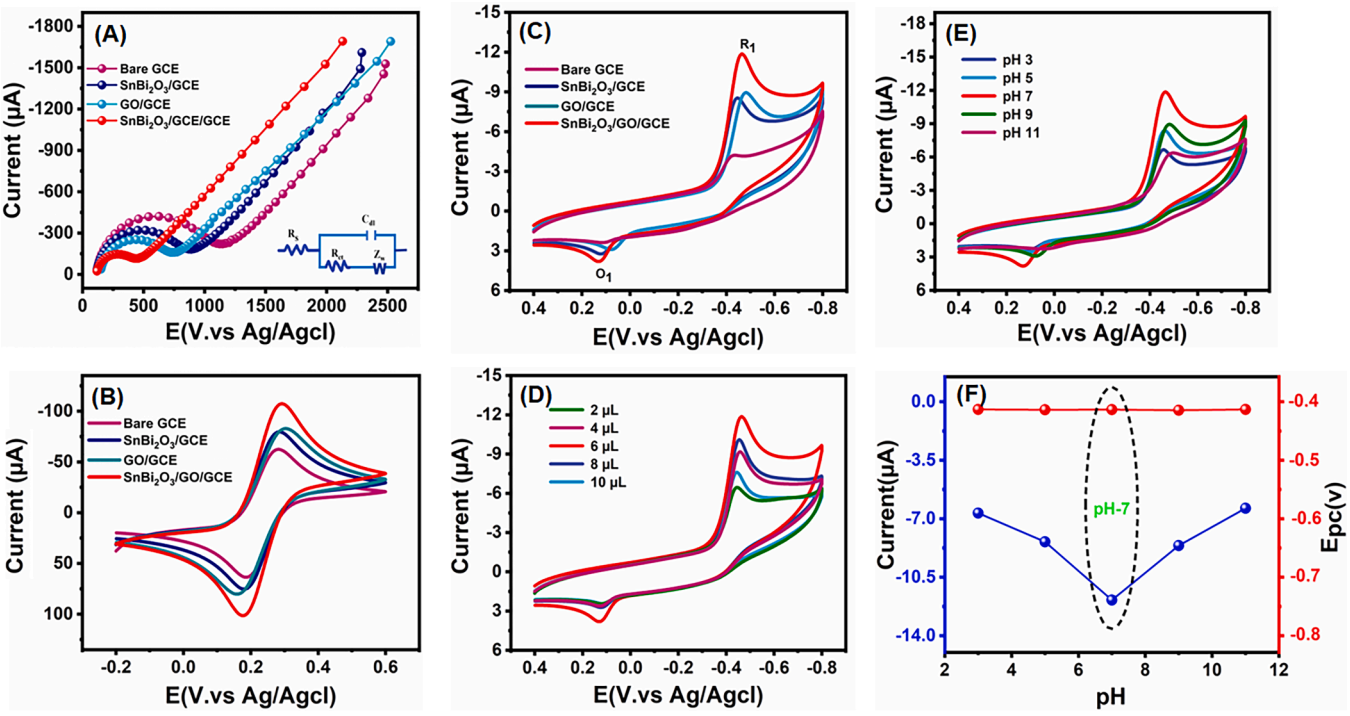

Fig. 3. (A) EIS spectrum of Bare GCE, GO/GCE, $SnBi_2O_3$/GCE, and $SnBi_2O_3$/GO/GCE in 0.5 M KCl and 5 mM $K_4[Fe(CN)_6]^{3-/4-}$ solution and (B) CV plots of the same electrodes under the same conditions. (C) CV responses of film comparison from Bare GCE, GO/GCE, $SnBi_2O_3$/GCE, and $SnBi_2O_3$/GO/GCE in 0.05 M PBS (pH 7.0) with 250 μM NF, scan rate at 50 mV/s. (D) CV curves showing the effect of varying $SnBi_2O_3$/GO volumes (2, 4, 6, 8, and 10 μL) on modified GCE in 0.05 M PBS (pH 7.0) in the presence of 250 μM NF, scan rate at 50 mV/s. (E) CV studies of $SnBi_2O_3$/GO/GCE in 0.05 M PBS at different pH values (3.0 to 11.0) with 250 μM NF, scan rate at 50 msV/s, and (F) The corresponding calibration plots of pH *vs*. Ipc (μA) and Epc (V).

consistently demonstrated that the $SnBi_2O_3$/GO/GCE electrode exhibited superior electrochemical behaviour, including higher peak currents, enhanced sensitivity, and better stability. This can be attributed to the synergistic effect, increased surface-active sites, larger surface area, presence of functional groups, unique structural features, and enhanced physicochemical properties. The irreversible cathodic peak corresponds to the reduction of the nitro group (R-NO_2) to hydroxylamine (R-NHOH), involving the transfer of four electrons and four protons [70]. Furthermore, during the reverse scan, an anodic peak is observed, indicating the oxidation of hydroxylamine, as seen in Scheme 2.

To optimize the electrode composition, $SnBi_2O_3$/GO electrodes were prepared with varying $SnBi_2O_3$-to-GO ratios (0.1 g/0.5 g, 0.2 g/0.5 g, 0.3 g/0.5 g, 0.4 g/0.5 g, and 0.5 g/0.5 g). Their electrochemical performance was evaluated in a 0.1 M PB (pH 7.0) using CV at a scan rate of 50 mV/s, as seen in **Fig. S 3**. The objective was to determine the optimal $SnBi_2O_3$ loading for achieving enhanced electrochemical response. Among the tested ratios, the 0.5 g/0.5 g composition exhibited the highest electrochemical performance, indicating that a well-balanced proportion of $SnBi_2O_3$ and GO significantly improves electrode sensitivity and overall efficiency. The performance of the modified electrode was optimized by varying the drop volume of active materials in 0.05 M PBS (pH 7.0) with the presence of 250 μM NF solution, with a scan rate of 50 mV/s in Fig. 3**D**. We tested different drop volumes (2, 4, 6, 8, and 10 μL) of a 6 mg/mL active materials suspension on the clean GCE surface. The resulting peak currents were noticed at 2 μL (−10.09 μA), 4 μL (−11.48 μA), 6 μL (−11.86 μA), 8 μL (−11.06 μA), and 10 μL (−9.14 μA), respectively. The peak current increased with drop volumes from 2 to 6 μL, indicating improved NF detection. However, drop volumes of 8 and 10 μL led to a decrease in peak current, likely due to an increased thickness of the active layer and less availability of active sites, which reduced interaction with the NF analyte. Thus, the optimal drop volume of 6 μL was selected, as it provided the most efficient response for NF detection. This optimized drop volume was used in all subsequent electrochemical studies.

In Fig. 3**E**, the effect of pH on the $SnBi_2O_3$/GO/GCE electrode for NF detection was studied across different pH levels, with measurements taken at a scan rate of 50 mV/s. The detection response of the $SnBi_2O_3$/GO/GCE electrode was evaluated in acidic, neutral, and basic conditions. The peak current values for NF detection were −10.62 μA, −10.69 μA, −11.86 μA, −10.67 μA, and −8.57 μA at pH 3.0, 5.0, 7.0, 9.0, and 11.0, respectively. In acidic conditions (pH 3.0 and 5.0), the NF detection current response varied by approximately ± 2 %. In contrast, in basic conditions (pH 9.0 and 11.0), the variation was about ± 3 %. The reduced response in basic conditions may be attributed to decreased interaction between the electrolyte and analyte due to increased negative charge. Therefore, the $SnBi_2O_3$/GO/GCE electrode exhibited the best performance for NF detection at a neutral pH of 7.0. Moreover, Fig. 3**F** illustrates the effect of different pH levels on potential values and peak currents. The linear regression equation for the cathodic peak potential (E_{pc}) vs different pH was calculated to be E_{pc}= 0.0034 V/ pH - 0.049,R^2 = 0.971. The slope value of 56 mV/pH unit for NF is close to the Nernstian theoretical value of 59 mV/pH unit, implying that an equal number of protons and electrons are transported onto the surface of the electrode, which is matched with previous studies. The data clearly show that the neutral pH 7.0 provides the most consistent and superior response compared to acidic and basic conditions. Consequently, pH 7.0 was used for all consequent electrochemical experiments.

Furthermore, Fig. 4A shows the CV curves depicting the effect of varying NF concentrations on the $SnBi_2O_3$/GO/GCE electrode. As the NF concentration increased from 50 to 250 μM, the oxidation peak current also increased. The peak current shifted negatively, which can be attributed to the increasing internal solution resistance caused by the higher NF concentration and the formation of an adsorption layer of NF on the electrode surface. Fig. 4B presents a calibration plot of NF concentration vs peak current response, yielding correlation coefficients of R^2 = 0.994 for reduction and R^2 = 0.9707 for oxidation. These results indicate that the $SnBi_2O_3$/GO composite material is highly efficient and sensitive to the electrochemical reduction of NF.

The CV curves of $SnBi_2O_3$/GO/GCE were recorded at different scan rates (20 to 200 mV/s) in the presence of 250 μM NF in 0.05 M PBS (pH 7.0). Fig. 4C shows that as the scan rate increases from 20 to 200 mV/s, the background current increases linearly, with a slight negative shift in peak potentials. The calibration plots of the square root of the scan rate vs. redox peak currents resulted in the following equations: (R_1) y = −27.074x - 3.352, R^2 = 0.9951, and (O_1) y = 11.701x + 0.7809, R^2 = 0.9911, as shown in Fig. 4D. These results indicate that the analyte detection on the $SnBi_2O_3$/GO/GCE surface is diffusion-controlled process. The $SnBi_2O_3$/GO/GCE demonstrates stable surface properties, making it an excellent candidate for further NF detection developments. Eq. (2) is used to determine the number of electrons involved in the irreversible electrode reaction [71,72]:

$$E_p = E^o + \frac{2.303\,RT}{\propto nF} log \frac{RTk^o}{\propto nF} + \frac{2.303\,RT}{\propto nF} \quad (2)$$

Where E^o is formal potential, v is scan rate (Vs^{-1}), R corresponds to the molar gas constant of 8.314 JK^{-1}, T is designated to the temperature (298 K), and n is standing for the number of electrons, $k^o$is the heterogeneous rate constant. As shown in Fig. S4, the log v vs. Ep graph shows good linearity for NF. The slope of the plot is 2.303RT/αnF, giving an αn = 3.80 for NF. For an irreversible electrode process, α is equal to 0.5. Using Eq. (2), the estimated number of electrons involved in the

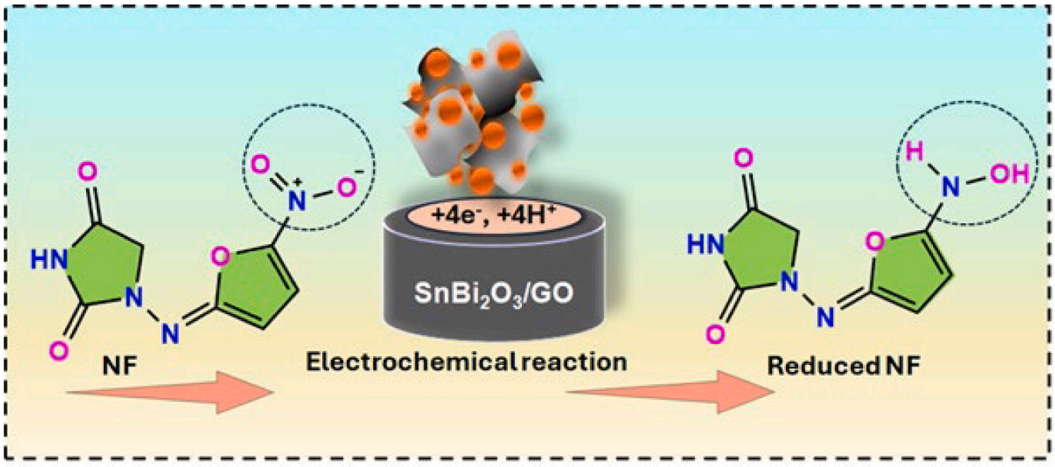

Scheme 2. The electrochemical reduction of NF over $SnBi_2O_3$/GO/GCE.

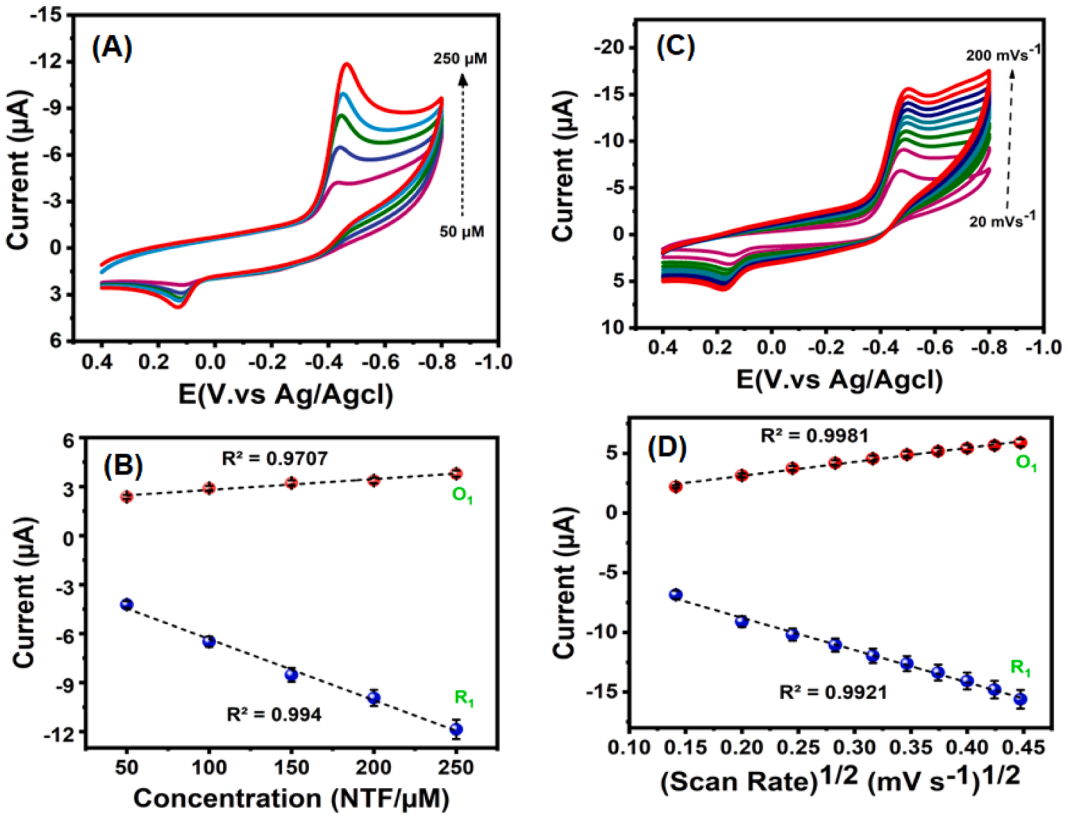

Fig. 4. (A) CV plots for NF concentrations ranging from 50 µM to 250 µM in 0.05 M PBS (pH 7.0) at a scan rate of 50 mV/s, and (B) the corresponding calibration plot of concentration (50 µM – 250 µM) vs. Ipc (µA). (C) CV plots for various scan rates (20 to 200 mV/s) in 0.05 M PBS (pH 7.0) with 250 µM NF, and (D) the corresponding linear plot of the square root of scan rate vs. redox peak current (O_1/R_1, µA).

reduction of NF is approximately 3.81, which is close to four. The reduction of NF involves the transfer of the equal number protons ($4H^+$) and electrons ($4e^-$).

3.2.3. *Detection response of NF from $SnBi_2O_3$/GO/GCE*

The DPV response of the $SnBi_2O_3$/GO/GCE composite toward NF reduction was investigated by applying a constant potential (*Epc*) ranging from +0.2 V to −0.6 V. NF was incrementally added to a nitrogen-saturated 0.05 M PBS solution (pH 7.0), and the corresponding reduction current was recorded. A stepwise increase in the reduction current, correlating to NF reduction, was observed, as shown in Fig. 5A. The inset figure, marked by an arrow, highlights the rapid response of $SnBi_2O_3$/GO/GCE within 40 seconds to a very low concentration of NF. The resulting linear range of detection was determined to be 0.023 to 814.36 µM. The regression equation for current (*Ipc*) vs. NF concentrations were determined as $Ipc = -0.0197\ C(mM) + 3.197$, with a correlation coefficient (R^2) of 0.9839. From this calibration curve, the sensitivity was calculated as 273.61 µA mM^{-1} cm^{-2} (From Eq. (3)), and the limit of detection (LOD) was found to be 0.0124 µM (From Eq. (4)). Furthermore, the selectivity of the $SnBi_2O_3$/GO/GCE composite, which is critical for efficient electrode performance in sensing applications, was evaluated and compared to previously report modified electrode performances, as summarized in Table 2.

$$Sensitivity = \frac{Slope\ of\ regression\ equation}{Working\ surface\ area\ of\ GCE} \quad (3)$$

$$LOD = 3\sigma / x \quad (4)$$

In this context, σ and π represent the standard deviation of the blank, where 3σ corresponds to three standard deviations, and 10π corresponds to ten standard deviations. The symbol x denotes the slope derived from the linear regression equation.

In Fig. 5C presents the DPV curve recorded in the presence of NF and various potential interferents such as GLU, DOP, UA, APAP, CAP, and metal ions like K^+, Ca^{2+}, Mg^{2+}, Na^+, and Zn^{2+} in the nitrogen-saturated 0.05 M PBS (pH 7.0) solution. The $SnBi_2O_3$/GO/GCE exhibited a distinct response to NF, while no significant response was observed for other interferents. These selective behaviours, as shown in Fig. 5D, confirm the electrode's specificity toward the target analyte.

3.2.4. *Repeatability, reproducibility and stability*

The CV studies were conducted to assess the repeatability, reproducibility, and storage stability of the $SnBi_2O_3$/GO/GCE electrode. First, the repeatability of the sensor was assessed by performing five consecutive measurements, yielding a relative standard deviation (RSD) of 2.14 % (Fig. 6A). The CV curve, shown in Fig. 6B, was recorded for the $SnBi_2O_3$/GO/GCE electrode in N_2-saturated 0.05 M PBS (pH 7.0) containing 200 µM NF. The measurements were performed using five independently prepared electrodes, resulting in a relative standard deviation (RSD) of 2.46 %, indicating good repeatability. For storage stability in Fig. 6(C), the modified electrodes were stored at room temperature for one week. Afterwards, the peak current response for 200 µM NF was measured at 6-day intervals, showing an RSD of 2.33 %, with 95.81 % of the initial response retained. These results confirm the excellent stability of the $SnBi_2O_3$/GO composite on the GCE. Overall, the $SnBi_2O_3$/GO/GCE electrode exhibited a well-defined electrocatalytic response towards NF.

3.2.5. *Real sample analysis*

To assess the performance and applicability of the $SnBi_2O_3$/GO/GCE sensors for the electrochemical detection of NF in real samples, measurements were conducted without and with human urine and tap water. The analysis was performed using DPV under phosphate buffer (pH 7.0) at a potential of 0.389 V. First, the control sample (unspiked

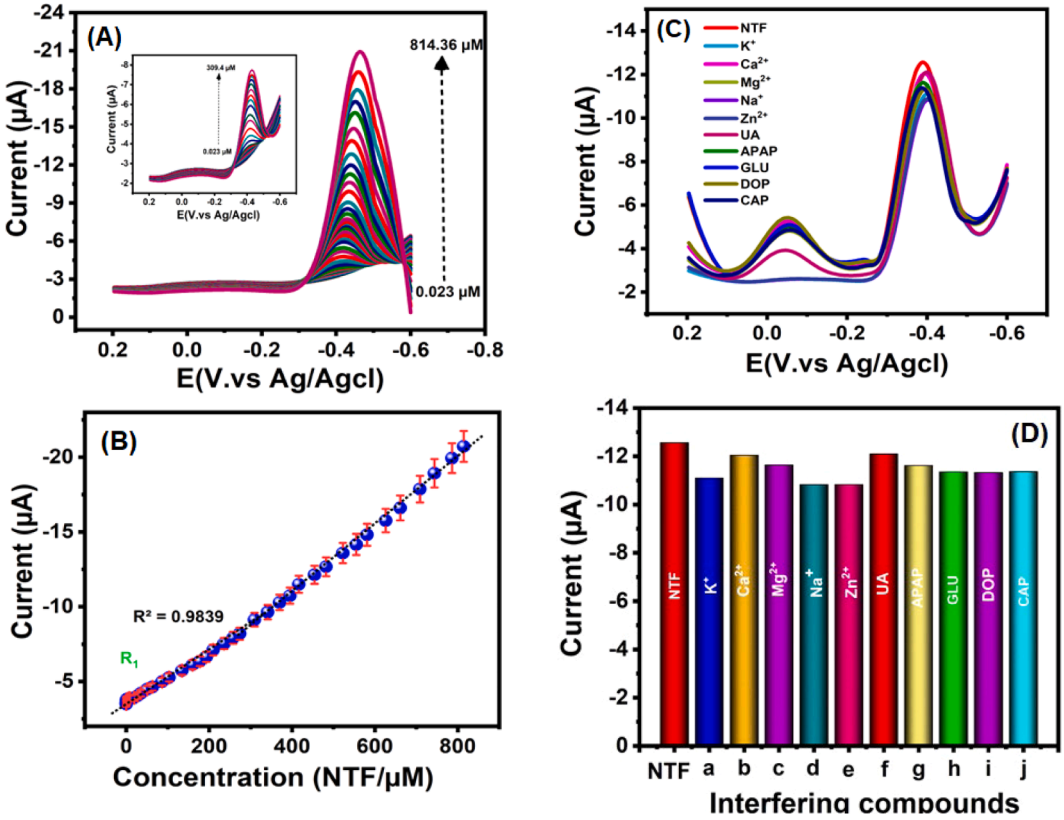

Fig. 5. (A) DPV responses of $SnBi_2O_3$/GO/GCE in 0.05 M PBS (pH = 7.0) for different NF concentration ranges, and (B) the corresponding calibration plot of NF reduction peak current (R1, µA) vs. concentration (µM). (C) DPV plots from interference studies showing the effect of various interfering molecules (at 20-fold concentration) on NF (20 µM) in 0.05 M PBS (pH = 7.0), and (D) a corresponding bar diagram of NF reduction current (µA) vs. interfering compounds.

Table 2
Comparison of $SnBi_2O_3$/GO/GCE sensors with previously reported materials for NTF detections.

Modified electrode	Method	Linear range (µM)	LOD (µM)	Ref.
NSO/GCE	*i-t*	0.006–466.67	3	[58]
rGO/Fe_3O_4/GCE	DPV	0.1–100	0.083	[73]
AuNPs/Gr/TFGE	DPV	0.2–4800	0.13	[74]
LMNSs/SPCE	DPV	0.010–144	0.072	[75]
DUT-67/T-PPY	DPV	9.08–1004.4	8.7	[76]
DS-DNA	DPV	2.5–37.5	0.8	[77]
Au-AuNR	*i-t*	3.0–500	0.18	[78]
Sg-C_3N_4/$CuWO_4$/GCE	DPV	50–610	6.51	[79]
$SnBi_2O_3$/GO/GCE	**DPV**	**0.023–814.36**	**0.0124**	**This work**

sample/without biological sample) concentrations of NF were conducted, and the sensor response for each control sample (Fig. 6D). The recovery percentage was calculated from the calibration of the detected current, yielding values between 99.86 % and 98.65 %, demonstrating the successful detection of NF, as seen in Table 3. Then, human urine samples were collected from Chang Gung Memorial Hospital (CGMH), Taiwan, adhering to the guidelines of the Chang Gung Biosafety Committee (contract number: 20210161B0) and in compliance with applicable laws and protocols and stored at 4 °C for use. Prior to analysis, the urine samples were centrifuged at 5000 rpm for 10 mins to remove any particulates and debris. The supernatant was diluted 1:10 (v/v) with deionized water to match the working concentration range of the sensor. The diluted urine sample was spiked with known concentrations of NF for the standard addition method and used directly for electrochemical analysis (Fig. 6E). Tap water was collected from a local source and filtered through a 0.22 µm membrane filter to remove suspended particles and impurities. The filtered tap water was used as is. Known concentrations of NF were spiked into the tap water samples for standard addition experiments (Fig. 6F). Both the prepared urine and tap water samples (spiked) were subjected to electrochemical analysis using the developed $SnBi_2O_3$/GO-modified electrode. Both urine and tap water samples were analysed using DPV to measure the sensor response. For each sample, triplicate measurements were performed to ensure accuracy and reproducibility. The recovery percentage was calculated from the calibration of the detected current, yielding values between 99.15 % and 97.14 % (Table 3), demonstrating the successful detection of NF in human urine and tap water with the $SnBi_2O_3$/GO/GCE sensor.

4. Conclusion

In summary, $SnBi_2O_3$ nanoparticles and GO nanolayers were successfully synthesized using hydrothermal methods. The $SnBi_2O_3$/GO nanocomposite was effectively prepared using an ultrasonication method. The physicochemical properties of the synthesized Sn-Bi_2O_3 nanoparticles, GO nanolayers, and $SnBi_2O_3$/GO nanocomposite were characterized using various spectroscopy techniques. The different modified electrodes were tested for NF detection, and the $SnBi_2O_3$/GO nanocomposite demonstrated high performance, selectivity, a wide linear range, and acceptable limits of detection. Additionally, $SnBi_2O_3$/GO/GCE showed good performance in spiked real samples of human urine and tap water, with DPV curves indicating reasonable response to additions. The $SnBi_2O_3$/GO/GCE exhibited excellent recovery performance in real sample analysis. We are developing $SnBi_2O_3$/GO/GCE for applications in the pharmaceutical industry.

CRediT authorship contribution statement

Krishnanpandi Alagumalai: Writing – original draft, Visualization, Validation, Formal analysis. **Nandhini Munusamy:** Methodology,

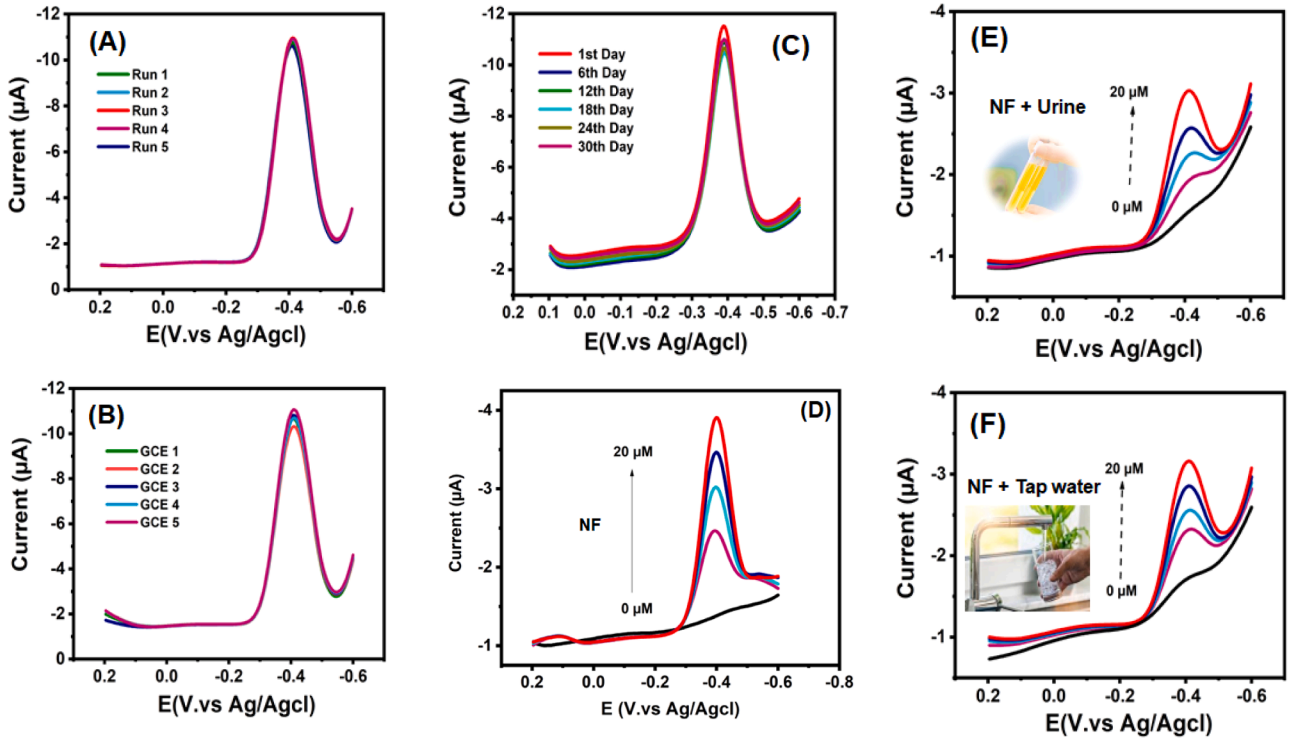

Fig. 6. DPV profile of $SnBi_2O_3$/GO/GCE for (A) repeatability, (B) reproducibility and (C) stability with presents of 200 μM NF in 0.05 M PBS (pH 7.0). DPV responses of $SnBi_2O_3$/GO/GCE for (D) spiked NF without (control sample) and with (E) human urine, (F) tap water.

Table 3
Real sample analysis of NF without and with urine and tap water (N = 3).

Sample	Added (μM/0.01 M)	Found (μM)	Recovery (%)
NF	0	—	—
	5	4.97	99.57
	10	9.86	98.65
	15	14.86	99.09
	20	19.93	99.66
NF + Human urine	0	—	—
	5	4.91	99.15
	10	9.85	98.72
	15	14.91	99.57
	20	19.24	98.17
NF + Tap water	0	—	—
	5	4.74	98.3
	10	9.03	97.64
	15	14.39	98.76
	20	19.68	98.62

*N-Replication.

Investigation, Data curation, Conceptualization. **Shen Ming Chen:** Funding acquisition. **Alangadu Kothandan Vivekanandan:** Writing – original draft, Visualization, Investigation. **Shih-Hsun Chen:** Formal analysis. **Mani Sivakumar:** Writing – original draft, Formal analysis. **Seong-Cheol Kim:** Funding acquisition. **B. Prakash:** Formal analysis.

Declaration of competing interest

The authors declare that they have no known competing financial interests or personal relationships that could have appeared to influence the work reported in this paper.

Acknowledgements

The authors express their appreciation for the funding provided by the National Science and Technology Council (NSTC) of Taiwan under project number MOST 113-2113-M-027-003. Also, this project was carried out with the support of the "2024 System Semiconductor Technology Development Support Project" of Chungbuk Technopark.

Supplementary materials

Supplementary material associated with this article can be found, in the online version, at doi:10.1016/j.jtice.2025.106033.

References

[1] aus der Beek T, Weber F, Bergmann A, Hickmann S, Ebert I, Hein A, Küster A. Pharmaceuticals in the environment—Global occurrences and perspectives. Environ Toxicol Chem 2016;35:823–35. https://doi.org/10.1002/etc.3339.
[2] Vivekanandan AK, Muthukutty B, Chen S-M, Sivakumar M, Chen S-H. Intermetallic compound Cu 2 Sb nanoparticles for effective electrocatalytic oxidation of an antibiotic drug: sulphadiazine. ACS Sustain Chem Eng 2020;8:17718–26. https://doi.org/10.1021/acssuschemeng.0c05629.
[3] Zhang G, Ju P, Lu W, Li A, Zhang Q, Jiang L, Zhang E. Rationally design a novel Zn-MOF for fluorescent detection of nitrofuran antibiotics: the synthesis, structure and sensing applications. Spectrochim Acta Part A Mol Biomol Spectrosc 2024;322:124836. https://doi.org/10.1016/j.saa.2024.124836.
[4] Su Y, Guo Y, Wu Q, Wang L, Wang Y, Yang G, Zhang W, Wang Y. Stable europium (III) metal–Organic framework fluorescence probe for intelligent visualization detection of gossypol and nitrofuran antibiotics in real samples. Inorg Chem 2024;63:15134–43. https://doi.org/10.1021/acs.inorgchem.4c02232.
[5] Sridharan G, Godwin CJT, Atchudan R, Arya S, Govindasamy M, Osman SM, Sundramoorthy AK. Iron oxide decorated hexagonal boron nitride modified electrochemical sensor for the detection of nitrofurantoin in human urine samples. J Taiwan Inst Chem Eng 2024;163:105320. https://doi.org/10.1016/j.jtice.2023.105320.
[6] Sivakumar M, Muthukutty B, Chen T-W, Chen S-M, Vivekanandan AK, Chen S-H, Hatshan MR, Ali MA, Kumar M. Electrocatalytic detection of noxious antioxidant diphenylamine in fruit samples with support of Cu@nanoporous carbon modified sensor. Chemosphere 2022;292:133400. https://doi.org/10.1016/j.chemosphere.2021.133400.
[7] Priyadarshanee M, Das S. Biosorption and removal of toxic heavy metals by metal tolerating bacteria for bioremediation of metal contamination: a comprehensive review. J Environ Chem Eng 2021;9:104686. https://doi.org/10.1016/j.jece.2020.104686.
[8] Mokarizadeh H, Sánchez-Montes I, Paul S, Hussain NAS, Moghrabi K, Stafford JL, Gamal El-Din M. Solar-activated tin oxide photocatalysis for efficient naphthenic

acids removal and toxicity reduction in oil sands process water. J Environ Chem Eng 2024;12:114168. https://doi.org/10.1016/j.jece.2024.114168.
[9] Mei Q, Ma B, Li J, Deng X, Shuai J, Zhou Y, Zhang M. Simultaneous detection of three nitrofuran antibiotics by the lateral flow immunoassay based on europium nanoparticles in aquatic products. Food Chem 2024;439:138171. https://doi.org/10.1016/j.foodchem.2023.138171.
[10] Mondal S, Alam N, Sarma D. Triazine core anchored lanthanide driven soft gels: photo switching emission, robust anticounterfeiting, and smart sensor probe for Nitroexplosive/Nitrofuran antibiotics. ACS Appl Eng Mater 2024;2:1467–82. https://doi.org/10.1021/acsaenm.3c00761.
[11] Srinithi S, Anupriya J, Chen S-M, Balakumar V. Ultrasonic fabrication of neodymium oxide@titanium carbide modified glassy carbon electrode: an efficient electrochemical detection of antibiotic drug nitrofurazone. J Taiwan Inst Chem Eng 2022;139:104522. https://doi.org/10.1016/j.jtice.2022.104522.
[12] Wang H, Xi H, Xu L, Jin M, Zhao W, Liu H. Ecotoxicological effects, environmental fate and risks of pharmaceutical and personal care products in the water environment: a review. Sci Total Environ 2021;788:147819. https://doi.org/10.1016/j.scitotenv.2021.147819.
[13] Nie J, Wang Q, Han L, Li J. Synergistic remediation strategies for soil contaminated with compound heavy metals and organic pollutants. J Environ Chem Eng 2024;12:113145. https://doi.org/10.1016/j.jece.2024.113145.
[14] Wang Y-N, Xu H, Wang S-D, Yang G-J, Jia Z-Y, Guo Z-Y, Zhang M-H, Wang Y-T, Wu T, Sun Z-H. Stable Cd(II)-based coordination polymer as a multifunctional fluorescent sensor for ascorbic acid, acetylacetone and nitrofuran antibiotics. J Mol Struct 2024;1315:138875. https://doi.org/10.1016/j.molstruc.2024.138875.
[15] Sabri NA, van Holst S, Schmitt H, van der Zaan BM, Gerritsen HW, Rijnaarts HHM, Langenhoff AAM. Fate of antibiotics and antibiotic resistance genes during conventional and additional treatment technologies in wastewater treatment plants. Sci Total Environ 2020;741:140199. https://doi.org/10.1016/j.scitotenv.2020.140199.
[16] Muthukutty B, Vivekanandan AK, Chen S-M, Sivakumar M, Chen S-H. Designing hybrid barium tungstate on functionalized carbon black as electrode modifier for low potential detection of antihistamine drug promethazine hydrochloride. Compos Part B Eng 2021;215:108789. https://doi.org/10.1016/j.compositesb.2021.108789.
[17] Vivekanandan AK, Subash V, Chen S, Chen S-H. Sonochemical synthesis of nickel-manganous oxide nanocrumbs decorated partially reduced graphene oxide for efficient electrochemical reduction of metronidazole. Ultrason Sonochem 2020;68:105176. https://doi.org/10.1016/j.ultsonch.2020.105176.
[18] Mitra S, Sultana SA, Prova SR, Uddin TM, Islam F, Das R, Nainu F, Sartini S, Chidambaram K, Alhumaydhi FA, Bin Emran T, Simal-Gandara J. Investigating forthcoming strategies to tackle deadly superbugs: current status and future vision. Expert Rev Anti Infect Ther 2022;20:1309–32. https://doi.org/10.1080/14787210.2022.2122442.
[19] Hsieh Y-T. Two-dimensional (2D) layered metal–Organic framework (MOF) composites as an electrochemical sensor for nitrofurans. ECS Meet Abstr MA2024-01 2024:2702. https://doi.org/10.1149/MA2024-01492702mtgabs. –2702.
[20] Afzal MH, Pervaiz W, Asif M, Huang Z, Dai J, Xu Y, Zhu J, Zhang T, Rao Z, Li G, Wang Z, Liu H. Engineering MXenes for electrochemical environmental pollutant sensing. Environ Sci Nano 2025;12:121–49. https://doi.org/10.1039/D4EN00255E.
[21] Schwarz S, Gildemeister D, Hein A, Schröder P, Bachmann J. Environmental fate and effects assessment of human pharmaceuticals: lessons learnt from regulatory data. Environ Sci Eur 2021;33:68. https://doi.org/10.1186/s12302-021-00503-0.
[22] Tamang SK, Gurung G, Parajuli RK, Yupeng B, Neupane K, Kipper MJ, Belfiore LA, Tang J. Smart sensing property of Eu3+-induced polyelectrolyte nanoaggregates on nitrofuran antibiotics in aqueous environments. J Environ Chem Eng 2024;12:114145. https://doi.org/10.1016/j.jece.2024.114145.
[23] Zhang S, Zhou Y, Tuo A, Chen S, Zhang Q, Zhang X, Xiong K, Gai Y. A stable viologen-based metal–Organic framework for fluorescence detection of nitroaromatics and nitrofuran antibiotics in water. Cryst Growth Des 2025;25:494–501. https://doi.org/10.1021/acs.cgd.4c01709.
[24] Mologni L, Daguer H, Hoff RB. Analysis of nitrofurans residues in foods of animal origin. Food toxicol. Forensics. Elsevier; 2021. p. 379–419. https://doi.org/10.1016/B978-0-12-822360-4.00015-7.
[25] Kaewnu K, Kongkaew S, Unajak S, Hoihuan A, Jaengphop C, Kanatharana P, Thavarungkul P, Limbut W. Portable smartphone-based aptasensor for nitrofuran detection. Microchem. J. 2024;200:110240. https://doi.org/10.1016/j.microc.2024.110240.
[26] Khanmohammadi A, Jalili Ghazizadeh A, Hashemi P, Afkhami A, Arduini F, Bagheri H. An overview to electrochemical biosensors and sensors for the detection of environmental contaminants. J Iran Chem Soc 2020;17:2429–47. https://doi.org/10.1007/s13738-020-01940-z.
[27] Qiu T, Jiang W, Bao S, Qian J, Wang C, Tang S, Shi X, Lu Y. Determination of persistent organochlorine pollutants in human serum by combining liquid-liquid extraction and solid-phase extraction with gas chromatography-tandem mass spectrometry. Microchem J 2024;197:109699. https://doi.org/10.1016/j.microc.2023.109699.
[28] Levy M, Al-Alam J, Delhomme O, Millet M. An integrated extraction method coupling pressurized solvent extraction, solid phase extraction and solid-phase micro extraction for the quantification of selected organic pollutants in air by gas and liquid chromatography coupled to tandem mass spectrome. Microchem J 2020;157:104889. https://doi.org/10.1016/j.microc.2020.104889.
[29] Baranwal J, Barse B, Gatto G, Broncova G, Kumar A. Electrochemical sensors and their applications: a review. Chemosensors 2022;10:363. https://doi.org/10.3390/chemosensors10090363.
[30] Alangadu Kothandan V, Mani S, Chen S, Chen S-H. Ultrasonic-assisted synthesis of nickel tungstate nanoparticles on poly (3,4-ethylene dioxythiophene):poly (4-styrene sulfonate) for the effective electrochemical detection of caffeic acid. Mater Today Commun 2021;26:101833. https://doi.org/10.1016/j.mtcomm.2020.101833.
[31] Saadati F, Ghahramani F, Shayani-jam H, Piri F, Yaftian MR. Synthesis and characterization of nanostructure molecularly imprinted polyaniline/graphene oxide composite as highly selective electrochemical sensor for detection of p-nitrophenol. J Taiwan Inst Chem Eng 2018;86:213–21. https://doi.org/10.1016/j.jtice.2018.02.019.
[32] Ahmed J, Faisal M, Harraz FA, Jalalah M, Alsareii SA. Porous silicon-mesoporous carbon nanocomposite based electrochemical sensor for sensitive and selective detection of ascorbic acid in real samples. J Taiwan Inst Chem Eng 2021;125:360–71. https://doi.org/10.1016/j.jtice.2021.06.018.
[33] Ensafi AA, Rezaloo F, Rezaei B. CoFe2O4/reduced graphene oxide/ionic liquid modified glassy carbon electrode, a selective and sensitive electrochemical sensor for determination of methotrexate. J Taiwan Inst Chem Eng 2017;78:45–50. https://doi.org/10.1016/j.jtice.2017.05.031.
[34] Rocha DP, Dornellas RM, Cardoso RM, Narciso LCD, Silva MNT, Nossol E, Richter EM, Munoz RAA. Chemically versus electrochemically reduced graphene oxide: improved amperometric and voltammetric sensors of phenolic compounds on higher roughness surfaces. Sensors Actuators B Chem 2018;254:701–8. https://doi.org/10.1016/j.snb.2017.07.070.
[35] Ali MA, Jiang H, Mahal NK, Weber RJ, Kumar R, Castellano MJ, Dong L. Microfluidic impedimetric sensor for soil nitrate detection using graphene oxide and conductive nanofibers enabled sensing interface. Sensors Actuators B Chem 2017;239:1289–99. https://doi.org/10.1016/j.snb.2016.09.101.
[36] Pal N, Chakraborty D, Cho E-B, Seo JG. Recent developments on the catalytic and biosensing applications of porous nanomaterials. Nanomaterials 2023;13:2184. https://doi.org/10.3390/nano13152184.
[37] Kannan P, Maduraiveeran G. Metal oxides nanomaterials and nanocomposite-based electrochemical sensors for healthcare applications. Biosensors (Basel) 2023;13:542. https://doi.org/10.3390/bios13050542.
[38] Ashjari M, Karimi-Maleh H, Ahmadpour F, Shabani-Nooshabadi M, Sadrnia A, Khalilzadeh MA. Voltammetric analysis of mycophenolate mofetil in pharmaceutical samples via electrochemical nanostructure based sensor modified with ionic liquid and MgO/SWCNTs. J Taiwan Inst Chem Eng 2017;80:989–96. https://doi.org/10.1016/j.jtice.2017.08.046.
[39] Ghiaci M, Tghizadeh M, Ensafi AA, Zandi-Atashbar N, Rezaei B. Silver nanoparticles decorated anchored type ligands as new electrochemical sensors for glucose detection. J Taiwan Inst Chem Eng 2016;63:39–45. https://doi.org/10.1016/j.jtice.2016.03.013.
[40] Xu L, Lin Z, Xiong X, Cheng H, Kang Z, Wang Y, Wu Z, Ma W, Yang N, He Y, Zou Z, Liu M, Li J, Kou X, Zhao Y. Surface enhancement effects of tiny SnO 2 nanoparticle modification on α-Fe 2 O 3 for room-temperature NH 3 sensing. Inorg Chem 2023;62:13649–61. https://doi.org/10.1021/acs.inorgchem.3c02116.
[41] Kuntoji G, Kousar N, Gaddimath S, Koodlur Sannegowda L. Macromolecule–Nanoparticle-based hybrid materials for biosensor applications. Biosensors (Basel) 2024;14:277. https://doi.org/10.3390/bios14060277.
[42] Selvi SV, Prasannan A, Yu H, Lincy V, Hong P-D. Bio-mineralized tin/bismuth oxide nanoparticles with silk fibroins for efficient electrochemical detection of 2-nitroaniline in river water samples. Environ Res 2023;221:115285. https://doi.org/10.1016/j.envres.2023.115285.
[43] Van Nguyen TH, Wu C-H, Lin S-Y, Lin C-Y. CoOx nanoparticles modified CuBi2O4 submicron-sized square columns as a sensitive and selective sensing material for amperometric detection of glucose. J Taiwan Inst Chem Eng 2019;95:241–51. https://doi.org/10.1016/j.jtice.2018.07.010.
[44] Madhale RA, Vhangutte PP, Kamble AJ, Bhange DS, Nerlekar NA, Dandge PB, Kulkarni A, Odam A, Bhange PD. Sn-doped Bi2WO6 for degradation of nitrophenol, Cr (VI) reduction and biomedical applications. J Taiwan Inst Chem Eng 2025;170:105997. https://doi.org/10.1016/j.jtice.2025.105997.
[45] Shen J, Zeng H, Chen C, Xu S. Novel plasmonic p-n heterojunction Ag-Ag2CO3/Bi2Sn2O7 photocatalyst for Cr(VI) reduction. J Taiwan Inst Chem Eng 2021;120:106–15. https://doi.org/10.1016/j.jtice.2021.02.025.
[46] Deepi A, Srikesh G, Nesaraj AS. Electrochemical performance of Bi2O3 decorated graphene nano composites for supercapacitor applications. Nano-Struct Nano-Obj 2018;15:10–6. https://doi.org/10.1016/j.nanoso.2018.03.003.
[47] Zhou J, Fan G, Ruan F, Li Y, Fan D, Chen Q. Construction of Bi2Sn2O7/Ag/Ag3PO4 heterojunction and its photocatalytic degradation properties. J Taiwan Inst Chem Eng 2022;138:104443. https://doi.org/10.1016/j.jtice.2022.104443.
[48] Liu H-Z, Han Q-F, Ding H-W, Yu H-M, Chiu T-W. One-step route to α-Bi2O3/BiOX (X = Cl, Br) heterojunctions with Bi2O3 ultrafine nanotubes closely adhered to BiOX nanosheets. J Taiwan Inst Chem Eng 2022;131:104147. https://doi.org/10.1016/j.jtice.2021.11.014.
[49] Jin W, Fu Y, Hu M, Wang S, Liu Z. Highly efficient SnS-decorated Bi2O3 nanosheets for simultaneous electrochemical detection and removal of Cd(II) and Pb(II). J Electroanal Chem 2020;856:113744. https://doi.org/10.1016/j.jelechem.2019.113744.
[50] Seaberg J, Clegg JR, Bhattacharya R, Mukherjee P. Self-therapeutic nanomaterials: applications in biology and medicine. Mater. Today. 2023;62:190–224. https://doi.org/10.1016/j.mattod.2022.11.007.
[51] Krishnapandi A, Muthukutty B, Chen S-M, Arul KT, Shiuan HJ, Selvaganapathy M. Bismuth molybdate incorporated functionalized carbon nanofiber as an electrocatalytic tool for the pinpoint detection of organic pollutant in life samples. Ecotoxicol Environ Saf 2021;209:111828. https://doi.org/10.1016/j.ecoenv.2020.111828.

[52] Wu D, Chen P, Feng D, Song J, Tong Y. Highly efficient electrochemical reduction of carbon dioxide to formate on Sn modified Bi2O3heterostructure. Dalt Trans 2021;50:14120–4. https://doi.org/10.1039/d1dt02586d.
[53] Adane WD, Chandravanshi BS, Tessema M. A pioneering electrochemical sensor for the simultaneous determination of nitrofurantoin and furazolidone residues in food and municipal wastewater samples. Sens Bio-Sens Res 2024;45:100678. https://doi.org/10.1016/j.sbsr.2024.100678.
[54] Munusamy N, Don Disouza FP, Chen S-M, Krishnan K, Jothinathan MKD, Prakash B. Facile fabrication of bismuth oxide anchored graphene oxide for the effective electrochemical sensing of diuron. J Taiwan Inst Chem Eng 2024;165:105708. https://doi.org/10.1016/j.jtice.2024.105708.
[55] Salih E, Mekawy M, Hassan RYA, El-Sherbiny IM. Synthesis, characterization and electrochemical-sensor applications of zinc oxide/graphene oxide nanocomposite. J Nanostructure Chem 2016;6:137–44. https://doi.org/10.1007/s40097-016-0188-z.
[56] Ruiz-Ramirez MM, Silva-Carrillo C, Hinostroza-Mojarro JJ, Rivera-Lugo YY, Valle-Trujillo P, Trujillo-Navarrete B. Electrochemical sensor for determination of nitrobenzene in aqueous solution based on nanostructures of TiO2/GO. Fuel 2021;283:119326. https://doi.org/10.1016/j.fuel.2020.119326.
[57] Maheshwaran S, Kogularasu S, Chen S-M, Chen W-H, Lee Y-Y, Chang-Chien G-P. Ultra-trace detection of sulfathiazole, an anti-infective agent and environmental contaminant, using electrochemical sensing with holmium vanadate-graphene oxide nanocomposites. J Taiwan Inst Chem Eng 2023;153:105233. https://doi.org/10.1016/j.jtice.2023.105233.
[58] Annalakshmi M, Sumithra S, Chen S-M, Chen T-W, Zheng X-H. Facile synthesis of ultrathin NiSnO 3 nanoparticles for enhanced electrochemical detection of an antibiotic drug in water bodies and biological samples. New J Chem 2020;44:10604–12. https://doi.org/10.1039/D0NJ01375G.
[59] Li X, Wu X, Li J, Huang J, Ji L, Leng Z, Qian N, Yang D, Zhang H. Sn-doped Bi 2 O 3 nanosheets for highly efficient electrochemical CO 2 reduction toward formate production. Nanoscale 2021;13:19610–6. https://doi.org/10.1039/D1NR06038D.
[60] Ganesamurthi J, Lee D, Muthukutty B, Juang R-S. Developing a ternary metal oxide Zn2GeO4 with graphitic carbon nitride supported nanocomposite for electrochemical assessment of nanomolar-scale nimesulide. J Taiwan Inst Chem Eng 2025;169:105986. https://doi.org/10.1016/j.jtice.2025.105986.
[61] Chen X, Qu Z, Liu Z, Ren G. Mechanism of oxidization of graphite to graphene oxide by the Hummers method. ACS Omega 2022;7:23503–10. https://doi.org/10.1021/acsomega.2c01963.
[62] Qayyum A, Batool Z, Fatima M, Buzdar SA, Ullah H, Nazir A, Jabeen Q, Siddique S, Imran R. Antibacterial and in vivo toxicological studies of Bi2O3/CuO/GO nanocomposite synthesized via cost effective methods. Sci Rep 2022;12:14287. https://doi.org/10.1038/s41598-022-17332-7.
[63] Al-Ghamdi AA, Al-Turki Y, Aal NA, Yakuphanoglu F, El-Tantawy F. Microwave—assisted hydrothermal synthesis of monoclinic bismuth trioxide nanorods: optical and photocatalytic properties. J Mater Sci Mater Electron 2017;28:8684–93. https://doi.org/10.1007/s10854-017-6593-3.
[64] Kusuma KB, Manju M, Ravikumar CR, Dileepkumar VG, Kumar AN, Santosh MS, Murthy HCA, Gurushantha K. Probe sonicated synthesis of bismuth oxide (Bi 2 O 3): photocatalytic application and electrochemical sensing of ascorbic acid and lead. J Nanomater 2022;2022. https://doi.org/10.1155/2022/3256611.
[65] Bhanjana G, Dilbaghi N, Kumar R, Umar A, Kumar S. Sno2 quantum dots as novel platform for electrochemical sensing of cadmium. Electrochim Acta 2015;169:97–102. https://doi.org/10.1016/j.electacta.2015.04.045.
[66] Manavalan S, Ganesamurthi J, Chen S-M, Veerakumar P, Murugan K. A robust Mn@FeNi-S/graphene oxide nanocomposite as a high-efficiency catalyst for the non-enzymatic electrochemical detection of hydrogen peroxide. Nanoscale 2020;12:5961–72. https://doi.org/10.1039/C9NR09148C.
[67] Afza N, Shivakumar MS, Krishnamurthy G, Mylarappa M, Ravikumar CR. Ni-doped cerium oxide on rGO: a hydrothermal approach for high-performance supercapacitors. Sustain Chem Environ 2024;6:100117. https://doi.org/10.1016/j.scenv.2024.100117.
[68] Basavaraja A, Ravikumar CR, Khan AA, Khasim S, Vasudeva B, Sharma S, Santosh MS. A sustainable combustion process for green synthesis of TiO 2 nanoparticles: applications in photocatalytic degradation and electrochemical sensing for environmental remediation. ChemistrySelect 2024;9. https://doi.org/10.1002/slct.202304910.
[69] Yang H, Zhou C, An J, Yang L, Yang Y, Liu X. Ultra-fast synthesis of iron decorated multiwalled carbon nanotube composite materials: a sensitive electrochemical sensor for determining dopamine. J Alloys Compd 2022;897:163257. https://doi.org/10.1016/j.jallcom.2021.163257.
[70] Akila B, Kanna Sharma TS, Sakthinathan S, Jana J, George M, Chiu T-W, Choi WM. Synthesis of functionalized boron nitride decorated on erbium vanadate (ErVO 4) composite for electrochemical detection of nitrofurazone in environmental samples. ACS Sustain Chem Eng 2024;12:6473–84. https://doi.org/10.1021/acssuschemeng.3c07518.
[71] J. Karende, Pdfft @ www.Sciencedirect.Com, (2017) 50–60. http://www.sciencedirect.com/science/article/pii/S0022519303003059/pdfft?md5=834312b8951197d76ea59366a57a94e6&pid=1-s2.0-S0022519303003059-main.pdf.
[72] Adane WD, Chandravanshi BS, Tessema M. Highly sensitive and selective electrochemical sensor for the simultaneous determination of tinidazole and chloramphenicol in food samples (egg, honey and milk). Sensors Actuators B Chem 2023;390:134023. https://doi.org/10.1016/j.snb.2023.134023.
[73] He B, Li J. A sensitive electrochemical sensor based on reduced graphene oxide/Fe 3 O 4 nanorod composites for detection of nitrofurantoin and its metabolite. Anal Methods 2019;11:1427–35. https://doi.org/10.1039/C9AY00197B.
[74] He B, Liu H. Electrochemical determination of nitrofuran residues at gold nanoparticles/graphene modified thin film gold electrode. Microchem J 2019;150:104108. https://doi.org/10.1016/j.microc.2019.104108.
[75] Karuppaiah B, Ramachandran R, Chen S-M, Wan-Ling S, Wan JY. Hierarchical construction and characterization of lanthanum molybdate nanospheres as an unassailable electrode material for electrocatalytic sensing of the antibiotic drug nitrofurantoin. New J Chem 2020;44:46–54. https://doi.org/10.1039/C9NJ05347F.
[76] Wang H, Bo X, Zhou M, Guo L. DUT-67 and tubular polypyrrole formed a cross-linked network for electrochemical detection of nitrofurazone and ornidazole. Anal Chim Acta 2020;1109:1–8. https://doi.org/10.1016/j.aca.2020.03.002.
[77] Ni Y, Wang P, Kokot S. Voltammetric investigation of DNA damage induced by nitrofurazone and short-lived nitro-radicals with the use of an electrochemical DNA biosensor. Biosens Bioelectron 2012;38:245–51. https://doi.org/10.1016/j.bios.2012.05.034.
[78] Rahi A, Sattarahmady N, Dehdari Vais R, Heli H. Sonoelectrodeposition of gold nanorods at a gold surface – Application for electrocatalytic reduction and determination of nitrofurazone. Sensors Actuators B Chem 2015;210:96–102. https://doi.org/10.1016/j.snb.2014.12.090.
[79] Srinivasan V, Kathiravan A, Kathiresan M, Krishnan G, Jhonsi MA. Facile synthesis of carbon nanocubes and its applications for sensing antibiotics. J Photochem Photobiol A Chem 2020;403:112855. https://doi.org/10.1016/j.jphotochem.2020.112855.